Development of a Photometer-based Aerosol Phase Functions for Simulating the Internal Radiation Field on Haze and Non-hazy Atmospheres

Written by

Mo Lan

A0073135M

Supervised by

Dr. Liew Soo Chin

Dr. Santo V. Salinas

A thesis submitted in partial fulfillment of the requirements for the degree of Bachelor of Science with Honours

Department of Physics

National University of Singapore

2013

Abstract

Atmospheric aerosols are among the major climate forcing agents. They interact directly by absorbing and scattering solar radiation as well as indirectly by acting as cloud seeds and influencing cloud lifetimes and Earth's hydrological cycle. However, given their importance from a climatological perspective, they are poorly characterized and understood, especially in regions for which Satellite or in-situ measurements remain a challenge. Over the last two decades and due to rapid economic growth, South- East Asia experiences mild to severe haze episodes generated from annual biomass burning, usually occurring during the dry season from June to October. In-situ aerosol measurements are now performed at the AERONET[1] site. Such measurements readily provide optical characterization of atmospheric aerosols, such as optical depth and Angstrom number, as well as retrievals of its physical properties, including single scattering albedo, phase functions etc. However, realistic aerosol phase functions can be quite complex and sometimes prohibitive to use in radiative transfer calculations that use Legendre expansion. This is mostly due to the fact that the expansion terms for realistic aerosol particles could be very large. In this thesis, a double Henyey-Greenstein approximation is adopted to generate aerosol phase functions inferred from the 1.5 level AERONET inversions. Numerical solutions to the radiative transfer equations for hazy and non-hazy atmospheres are evaluated and compared to see if there is difference in aerosol phase functions between hazy and non-hazy conditions. Level 1.5 AERONET inversions for year 2008 and year 2010 were obtained and processed in this study.

[1] Aerosol Robotic Network [http://aeronet.gsfc.nasa.gov]

Acknowledgments

I would like to express my sincere appreciation and gratefulness to Dr. Liew Soo Chin and Dr. Santo V. Salinas from the Centre for Remote Imagining, Sensing and Processing (CRISP) for their endless support, understanding and guidance that helped me overcome every theoretical and technical difficulty. I learn so much not only from their extensive knowledge in Physics but also their genuine attitude towards research and work. I want to express my special thanks to Michael Mishchenko at the NASA Goddard Institute for Space Studies, who developed the T-Matrix Mie scattering code that I used to process raw data generate aerosol phase functions. I would also thank my friends Li Shiying, He Yingshu and Chen Lingzi, for their company in numerous late nights. Finally, I would like to thank my family for their constant love and support.

Contents

1 Introduction

1.1 Aerosol content and haze

Aerosols are small, airborne solid and liquid particles suspended in the atmosphere. They interact both directly and indirectly with the Earth's radiation budget and climate. As a direct effect, the aerosols scatter sunlight directly backs into space. As an indirect effect, aerosols in the lower atmosphere can modify the size of cloud particles, changing how the clouds reflect and absorb sunlight, thereby affecting the Earth's energy budget. They are found mostly in the lower 2km of the atmosphere. When aerosols are large enough, they can absorb and scatter sunlight. This scattering mechanism can reduce visibility (haze) and redden sunrises and sunsets [1, 2].

The source of haze in Singapore comes mostly from biomass burning occurring seasonally in Sumatra, Indonesia [3, 4]. From the ARONET data records, as shown in Figure 1, it is observed that in a clear atmosphere, the overall aerosol concentration is low, and aerosol size distribution evenly peaks around 0.1 μm and around 5μm and with a low concentration of aerosol particles. However, for haze periods, the overall aerosol concentration increases and the aerosol size distribution peaks at the small particle size range (between 0.1 to 1.0μm).

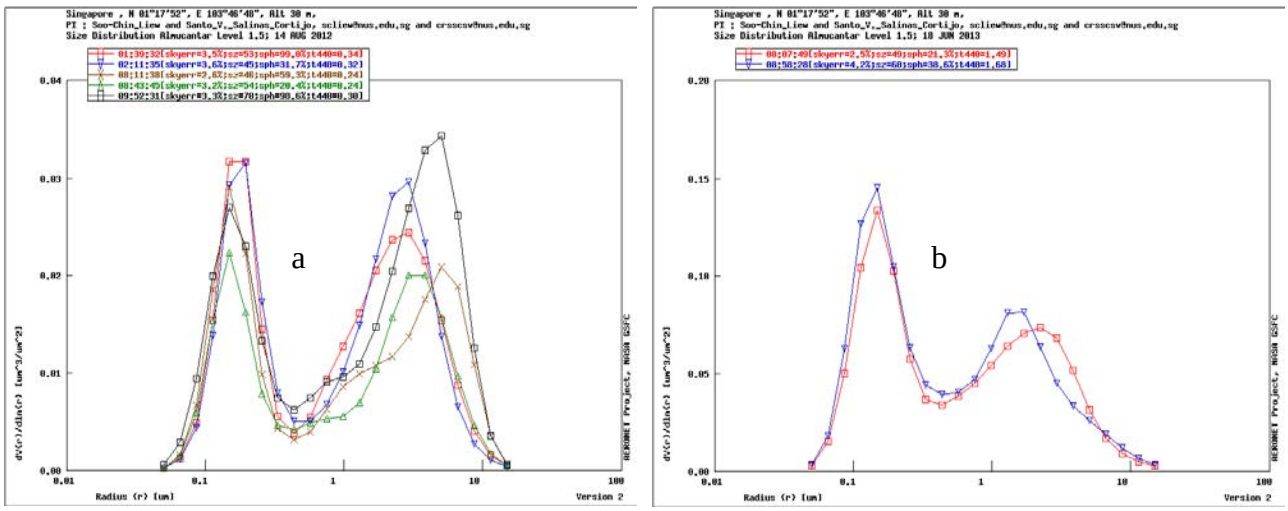

Figure 1. An example of aerosol size distribution in (a) non-hazy and (b) hazy atmosphere.

In Singapore, the pollution standard index (PSI) is used by the National Environmental Agency (NEA) to describe the relative quality of atmosphere. The PSI is based on six pollutants particulate matter (PM10), fine particulate matter (PM2.5), sulphur dioxide (SO2), carbon monoxide (CO), ozone (O3) and nitrogen dioxide (NO2) [5]. The process of biomass burning produces CO, PM10 and PM2.5 and results in a drastic increase in small aerosol concentration. During periods of haze, this increase is consistent observed with the help of a Sun-photometer and recorded by the AERONET network.

From 2009 onwards, The National Environment Agency started to update daily pollution standard index (PSI) online, especially during the annual dry season from June to October when haze occurs. Besides that, reducing visibility in hazy weather could largely affect traffic and outdoor activities. Therefore, it is very important to understand the physical and optical characteristics of biomass burning aerosols as well as their scattering properties during haze and non-haze periods.

1.2 Objective

There are two purposes of this project. The primary purpose is to reduce the complexity (i.e. Legendre expansion terms) in the generation of phase functions in order to shorten the processing time for large photometric data sets. The secondary purpose of the project is to investigate if there is a difference in aerosol scattering phase functions between hazy and non-hazy atmosphere and try to explain the differences.

1.3 Scope

This thesis starts with an introduction of aerosol and haze to provide some background information. The main body of the thesis consists of three parts: theory, methodology and results and discussion, followed by conclusion and references.

2 Theory

2.1 Scattering by a single particle

Matter is composed of discrete electric charges: electrons and protons. When a beam of light encounters a particle, the oscillating electric field of the incident light induces electric dipoles in the particle. The dipoles oscillate at the same frequency as the incident field. These oscillating charges radiate electromagnetic waves in all directions. These re-radiated electromagnetic waves are known as the scattered radiation. In addition to re-radiating electromagnetic energy, the excited elementary charges may transform part of the incident electromagnetic energy into other forms. This process is called absorption. [6] The electric field of the scattered wave at a point along a particular direction is the sum of all the waves radiated from all sections of the particle, taking into account the phase differences. If the particle is small compared with the wavelength of the incident wave, all these waves are in phase and the particle can be considered to radiate as a single oscillating dipole. If the particle is large, there are interference effects due to the phase differences of the scattered waves originated from different parts of the particle, and the scattered wave field is more complicated.

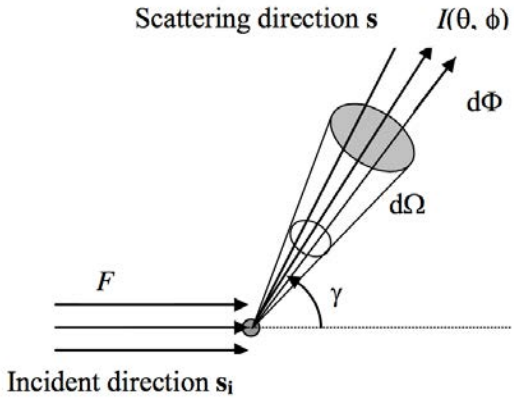

Figure 2. A sample of light scattering

Assume a particle encounters a parallel beam of light, with flux F along the incident direction $s_i(\theta_i\phi_i)$. This beam of light is partially absorbed and partially scattered by the particle. The

sensor is placed to receive scattered light within a small cone of solid angle $d\Omega$ at a scattering angle γ with respect to the incident beam.

$$cos\gamma = \boldsymbol{s} \cdot \boldsymbol{s_i} \tag{1}$$

The intensity of the scattered light in a particular direction is direction dependent,

$$I(s, s_i) = \frac{d\Phi}{d\Omega} \tag{2}$$

The total flux scattered is an integral over all directions.

$$\Phi_s = \int_{\substack{all \\ directions}} I(\gamma, \phi) d\Omega = \int_0^{2\pi} \int_0^{\pi} I(\gamma, \phi) sin\gamma d\gamma d\phi \tag{3}$$

Scattering cross-section σ_s is defined as the total scattered flux per unit incident flux density

$$\sigma_s = \frac{\Phi_s}{F} \tag{4}$$

When the refractive index contains a non-zero imaginary part, absorption occurs. The absorption cross-section σ_a is defined as the total absorbed flux per unit incident flux density

$$\sigma_a = \frac{\Phi_a}{F} \tag{5}$$

For convenience, ratio of scattering and absorption cross-sections to the geometric cross-section A_g is defined as scattering efficiency and absorption efficiency.

$$Q_s = \frac{\sigma_s}{F} \qquad Q_a = \frac{\sigma_a}{F} \tag{6}$$

The extinction cross-section and extinction efficient are the sums of scattering and absorption cases

$$\sigma_e = \sigma_s + \sigma_a \qquad Q_e = Q_s + Q_a \tag{7}$$

The single scattering albedo ω of the particle is defined as the ratio of the scattering cross-

section to the extinction cross-section

$$\omega = \frac{\sigma_s}{\sigma_s + \sigma_a} \tag{8}$$

2.2 Particle scattering phase function

The particle scattering phase function describes the angular distribution of the reflected incoming solar radiation and it depends on the particle size, shape and refractive index of the scattering particle. Values of phase function for a given scattering angle are proportional to the probability that an incident light beam will be scattered in a certain direction.

The forward scattering direction refers to the range of scattering angles $0 < \gamma < \pi/2$ while the backward scattering direction refers to $\pi/2 < \gamma < \pi$. The fractions of forward scattering and backward scattering are

$$f_{forward} = \frac{1}{4\pi} \int_0^{2\pi} \int_0^{\pi/2} P(\gamma)\, sin\gamma d\gamma d\phi \tag{9}$$

$$f_{backward} = \frac{1}{4\pi} \int_0^{2\pi} \int_{\pi/2}^{\pi} P(\gamma)\, sin\gamma d\gamma d\phi \tag{10}$$

$$f_{forward} + f_{backward} = 1 \tag{11}$$

For particles that are much smaller that the incident wavelength, the phase function is symmetric in the forward and backward direction. Scattering by small particles is known as Rayleigh scattering. The Rayleigh phase function can be described as

$$P(cos\gamma) = \frac{3}{4}(1 + cos^2\gamma) \tag{12}$$

Scattering by large particles with size comparable to incident wavelength is known as Mie Scattering. The Mie scattering cross section and phase function can be computed for a homogenous sphere and a few other particles of simple geometry. [7] The shape of the phase function depends on the particle size. Typically, the phase function has a narrow forward

scattering peak with several side lobes and a wider and much smaller backscattering peak. The larger the particle size, the narrower is the forward scattering peak. Unlike Rayleigh scattering, Mie scattering phase functions generally cannot be represented by simple analytic functions.

An important parameter that characterizes the degree of symmetry (or asymmetry) "g" of the phase function is the mean value of the cosine of the scattering angle and using the phase function as the weighting function.

$$g = < cos\gamma > = \frac{\int_0^{2\pi} \int_{-1}^{1} P(\gamma, \phi)\, cos\gamma d(cos\gamma) d\phi}{\int_0^{2\pi} \int_{-1}^{1} P(\gamma)\, d(cos\gamma) d\phi} \tag{13}$$

In the case of azimuthal symmetry, i.e. for Rayleigh scattering, if the phase function is symmetric about $\gamma = \pi/2$, then it can be seen from the above equation (13) that g = 0. If the phase function is narrowly peaked in the forward direction, then g has a value close to one. On the other hand, if the phase function is peaked in the backward direction, g has a negative value.

Since Mie scattering function can be very complicated, it is often convenient to have a simple analytic formula that approximates the shape of actual phase functions. One commonly used approximation is the Henyey-Greenstein Phase Function. It takes a form of

$$P(\gamma) = \frac{1 - g^2}{(1 + g^2 - 2g cos\gamma)^{3/2}} \tag{14}$$

Where g is the asymmetry of this specific phase function. For a more realistic representation of aerosol particles, in this thesis, a double Henyey-Greenstein Phase Function is used to obtain better approximation. In this case, the phase function is a linear combination of forward and backward scattering components with the equation

$$P(\gamma) = f \frac{1 - g_1^2}{(1 + g_1^2 - 2g_1 cos\gamma)^{3/2}} + (1 - f) \frac{1 - g_2^2}{(1 + g_2^2 - 2g_2 cos\gamma)^{3/2}} \tag{15}$$

Where *f* is the fraction of forward scattering, g_1 and g_2 are the asymmetricity associated with forward and backward scattering respectively.

2.3 Scattering matrix for an ensemble of particles

A scattering matrix relates the electric field of the scattered wave to that of the incident wave. All exact techniques for calculating electromagnetic scattering are based on solving the differential Maxwell equations or their integral counterparts in the time or frequency domain, either analytically or numerically. There are various models and different approaches to calculate scattering matrices, such as K. F. Evans and G. L. Stephens's model (1991)[8], and Hapke model (1993) [9] and Michael model (1999) [10].

In this project, the Mie phase functions are generated using T-Matrix program [6, 7, 13, 14] that computes far-field light scattering by poly-disperse homogeneous spherical particles using the Lorenz-Mie theory. Which solves Maxwell equations. The Fortran code used in the computation is spher.f code developed by Michael Mishchenko at the NASA Goddard Institute for Space Studies.

2.4 The Radiative Transfer Equation (RTE)

In order to simulate the internal radiation field inside a scattering atmosphere we need to solve the radiative transfer equation (RTE) for a model atmosphere. For our purpose we solve the RTE vertically homogeneous plane-parallel scattering atmosphere. The solution method used in this work is the Doubling and Adding (D&A) method that is briefly described below and found in the work of [8].

First we express the angular aspects of the radiance field by a vector in a radiance basis. The scattering source integral in the radiative-transfer equation is correspondingly represented by matrix multiplication. Therefore the matrix differential equations can be integrated with the doubling and adding method, starting from infinitesimal layers of a prescribed atmosphere.

In general, the monochromatic plane-parallel polarized radiative transfer equation for randomly oriented particles can be described as

$$\mu \frac{dI(\tau,\mu,\phi)}{d\tau} = -\boldsymbol{I}(\tau,\mu,\phi) + \frac{\widetilde{\omega}}{4\pi}\int_0^{2\pi}\int_{-1}^{1} \boldsymbol{\mathcal{M}}(\mu,\phi;\mu',\phi)\boldsymbol{I}(\tau,\mu',\phi)d\mu' d\phi' + \sigma(\tau,\mu,\phi) \quad (16)$$

Where **I** is the diffuse radiance field expressed as a four-vector of Stokes parameters (*I, Q, U, V*), $\tilde{\omega}$ is the single scattering albedo, τ is the optical depth, μ is the cosine of the zenith angle, ϕ is the azimuth angle and $\boldsymbol{\mathcal{M}}$ is the 4×4 scattering matrix, σ is the stokes vector of radiation sources, in this case, downward τ increases and μ is positive for downward directions. There are two sources of radiation, one is the thermal emission, and the other comes from single scattered solar radiation. The strokes vector can be expressed as

$$\sigma(\mu,\phi) = (1-\tilde{\omega})B(T)\begin{bmatrix}1\\0\\0\\0\end{bmatrix} + \frac{F_0}{\mu_0}\frac{\tilde{\omega}}{4\pi}exp(-\tau/\mu_0)\boldsymbol{\mathcal{M}}(\mu,\phi;\mu_0,\phi_0)\begin{bmatrix}1\\0\\0\\0\end{bmatrix} \quad (17)$$

In this equation, *B(T)* is the Planck blackbody function, the first term is the thermal emission component and the second term is the single scattered solar radiation: F_0 stands for unpolarized solar flux at the top of the atmosphere, and $(\mu_0, \phi_0)$is the direction of the collimated solar beam.

Radiation varies in different angles. This angular variation can be expressed by a Fourier series in azimuth and by discretization in zenith angle using numerical quadrature. There are several types of numerical quadrature available for this model: Gaussian, Lobatto and double Gaussian schemes. The radiance at a particular optical depth can be expressed by a vector in a radiance basis which involves stokes parameters, quadrature zenith angles and Fourier azimuth modes as its three components.

Radiance Field can be consider separately according to hemisphere. I^+ represents downward radiance when μ is positive; and I^- represents upward radiance when μ is negative. Stoke parameters describes the polarization state of electromagnetic radiation, therefore the number of Stokes parameters depends on number of polarization terms, which could be less than four. For Stokes parameter in this project, polarization is not considered and there is only one value. The number of quadrature angles and azimuth modes can be modified to get a desired accuracy of the radiance field.

Interaction principle expresses the linear interaction of radiation with a medium. For example, the radiation emerged from a layer is related to the radiation incident upon the layer and the

radiation generated within the layer (i.e. thermal emission). The interaction principle can then be expressed in terms of a radiance vector

$$I_1^- = T^+ I_0^+ + R^+ I_1^- + S^+$$
$$I_0^+ = T^- I_1^- + R^- I_0^+ + S^- \quad (18)$$

T is the transmission matrix, R is the reflection matrix and S is the source vector. For the whole atmosphere, computing R, T and S individually and summing them up according to the interaction principle can solve the radiative transfer equation of the atmosphere. Besides, it is easy to relate R, T and S for an infinitesimal layer to the single scattering properties. Hence the solution method of RTE consists of two parts: first, the single scattering information is converted into a form suitable for applying interaction principle; second, compute the properties of the entire atmosphere based on the infinitesimal properties using adding and doubling method. [8]

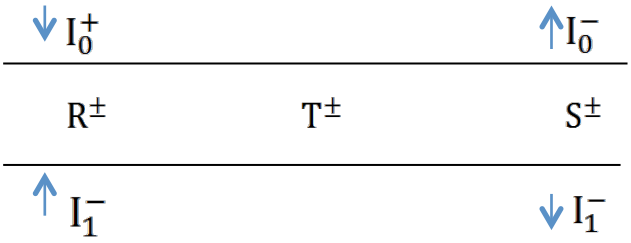

Figure 3. A schematic illustration of the interaction principle. I_0^+ and I_1^- represent the incident radiation received by the layer of atmosphere. I_0^- and I_1^+ represent the emergent radiation.

3 Data analysis

3.1 Overview

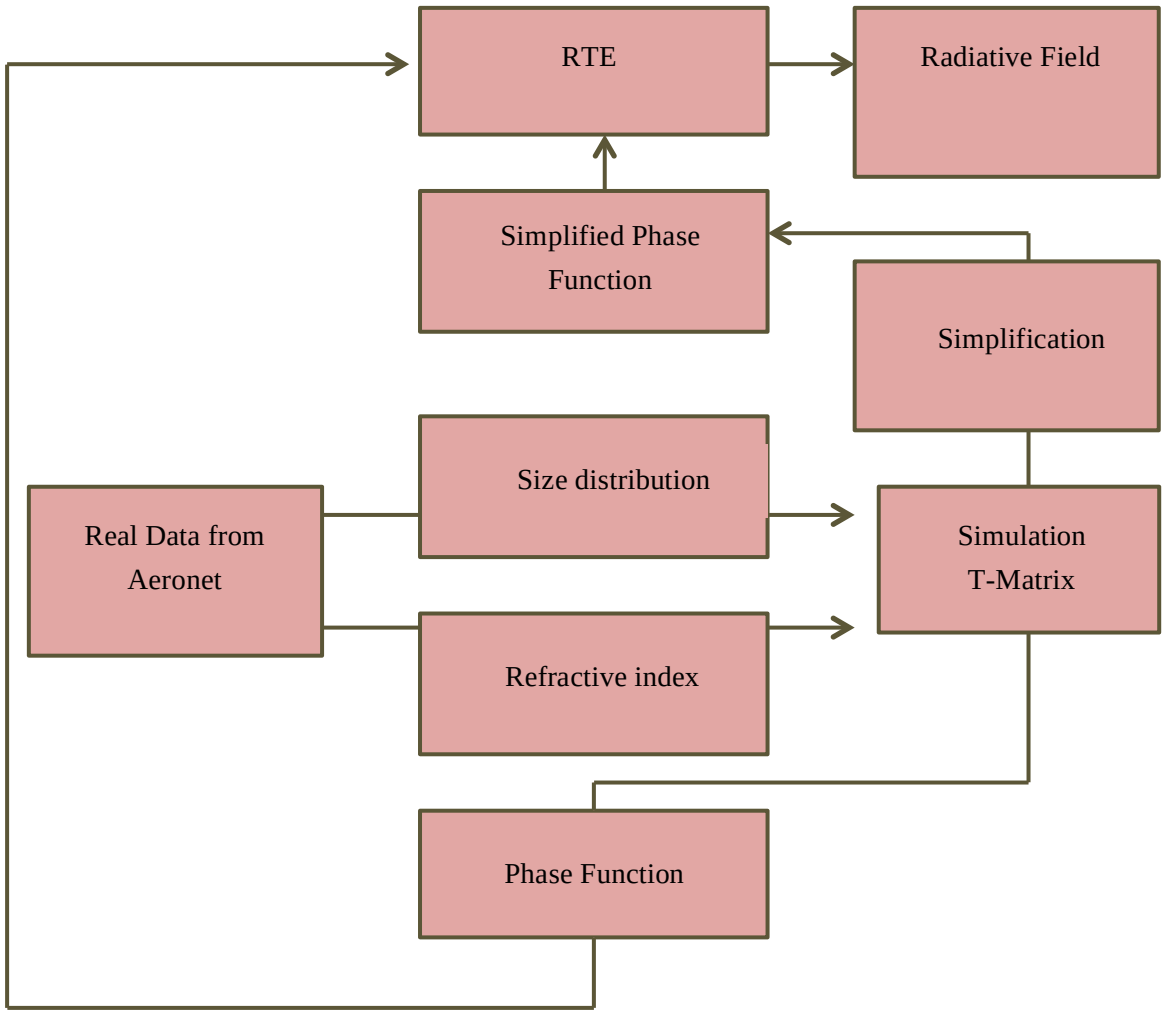

Figure 4. A flow chart of data analysis process.

3.2 Choice of raw data

There are 3 levels of data in AERONET. Level 1.0 data which is non cloud screened, level 1.5 data from AERONET is cloud screened by not quality-assured, and only the level 2.0 is both cloud screened and quality-assured. The data used in this project is level 1.5 data because Singapore's AERONET site only started to function in 2006, there are still many calibration and adjustments to be down to assure an accurate and consistent data collection. Therefore there are not enough level 2.0 data to cover both hazy and non-hazy periods.

In order to improve the quality of data, data from 2006 and 2007 was not considered as there were still many errors at the beginning years and there are months with no data records. Data of Year 2008 and 2010 was chosen as they have a mostly complete data set over the entire year. Furthermore, after two years of calibration, the data collection becomes relatively stable. To better ensure the quality of data, manual screening is done to remove all the readings with more than 5% error. Daily and monthly averages are taken to reduce fluctuations and extreme readings.

3.3 Aerosol size distribution fitting

Monthly averages of aerosol size distribution and refractive index (both real and imaginary parts) are obtained for year 2008 and 2010. The annual data is grouped into two periods, hazy and non-hazy. Then non-hazy period last from February to July and the hazy period usually starts from August to November. However, instead of using real data which might be scattered and contain irregular patterns, it is often convenient to approximate natural size distributions using simple analytical distribution functions. Mishchenko suggested six analytical size distributions. Among them, the modified bimodal log normal distribution was chosen as it best represents the two peaks in the size distribution graph. Useful information was obtained from the fitting and used to generate Mie phase functions in T-matrix [7].

The approximate equation is

$$n(r) = \text{constant} \times \left\{ exp\left[-\frac{(lnr - lnr_{g1})^2}{2ln^2\sigma_{g1}} \right] + \gamma exp\left[-\frac{(lnr - lnr_{g2})^2}{2ln^2\sigma_{g2}} \right] \right\} \quad (19)$$

Where r is the radius of aerosol particle, r_{g1} and r_{g2} is the radius at two peaks, σ_{g1} and σ_{g2} are the full width at half maximum (FWHM) for both peaks and gamma is the ratio of amplitude at r_{g1} over amplitude at r_{g2}.

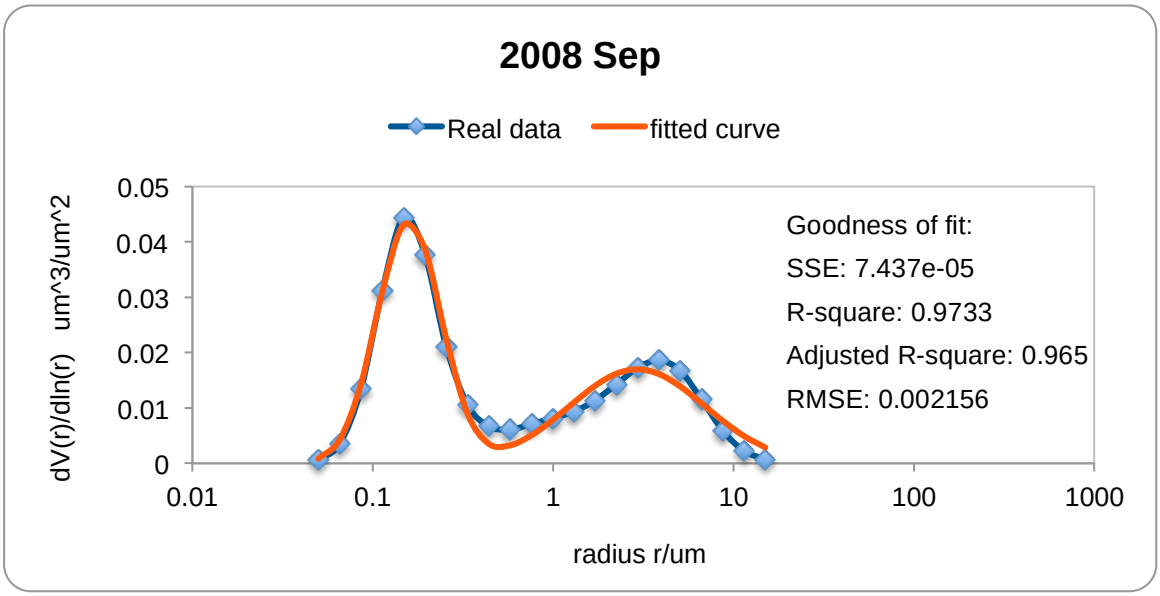

Figure 5. A sample of fitted size distribution curve

For example, as shown in figure 5, the R-square value is 0.9733 for September 2008 and RMSE is less than 0.01. The approximation fits very closely to the real data, especially for small particle peak on the left. Beside, in this graph, the peak at small radius has a higher amplitude compare to the one for larger particles, indicating a higher concentration of small particles, which is mostly due to biomass burning. Values of r_{g1}, r_{g2}, σ_{g1}, σ_{g2} and gamma obtained from the approximation are used in T-matrix to generate the Mie phase function

3.3 Refractive index

Daily and monthly averages of refractive index are calculated. The real part represents scattering and the imaginary part represents absorption during the transmission process. The numerical values of refractive indices are shown in the following table.

	2008 Real part	**2008 Imaginary**	**2010 Real part**	**2010 Imaginary**
Non-hazy	1.417792917	0.010383976	1.407031643	0.008366495
Aug	1.418694762	0.006828429	1.398852778	0.010957028
Sep	1.4449	0.0141565	1.420895833	0.008504375
Oct	1.355166667	0.013819667	1.429183333	0.0113575
Nov	1.45235	0.025205	1.412075	0.00719375

Table 1. Monthly average refractive index of 2008 and 2010

Large imaginary part of refractive index indicates a high absorption during light transmission and hence often corresponds to hazy atmosphere. The imaginary refractive index of September 2008 is small and the aerosol size distribution is showing a high concentration of small aerosol particles. Readings of refractive index are consistent with the aerosol content. However, although the imaginary refractive index of November 2008 is extraordinary high, the aerosol size distribution graph does not agree with it. This is because there was only one valid data point in November 2008. Although the error of this data point is below 5%, a single reading may not represent the general condition. Therefore the value of imaginary part of November 2008 can be considered as an anomaly.

3.4 Generation of Phase Function

With all the inputs available, phase functions are computed using T-matrix. The numerical sample of an output of phase functions is shown in table 2. Besides the direct radiation F11, this output also includes polarizations F33, F12 and F34, but polarization is not considered in this project.

Angles	F11	F33	F12	F34
0	80.95953	80.95953	0	0
5	14.77673	14.76672	0.00389	0.31007
10	7.51231	7.49477	-0.03419	0.18924
15	5.62667	5.60819	-0.07768	0.13468
20	4.6778	4.65996	-0.12506	0.12159
25	3.97608	3.95592	-0.17318	0.12572
30	3.37423	3.34876	-0.21848	0.1342
35	2.84014	2.80675	-0.25763	0.14098
40	2.36881	2.32517	-0.28838	0.14345
45	1.95962	1.90388	-0.30965	0.14099
50	1.61064	1.54147	-0.32142	0.13402
55	1.31791	1.23448	-0.32446	0.12342
60	1.0759	0.97783	-0.32006	0.11024
65	0.8783	0.76561	-0.30966	0.09556
70	0.71864	0.59157	-0.29468	0.08022
75	0.59085	0.44984	-0.27649	0.0649
80	0.4894	0.33492	-0.25623	0.05015
85	0.40949	0.24202	-0.23479	0.03629
90	0.34702	0.16696	-0.21292	0.02355
95	0.29863	0.10626	-0.19115	0.01207
100	0.26155	0.05697	-0.16986	0.00192
105	0.23358	0.01668	-0.14932	-0.00689
110	0.21294	-0.01657	-0.12968	-0.01437
115	0.19829	-0.0444	-0.11107	-0.02053
120	0.18854	-0.06809	-0.09354	-0.02541
125	0.18288	-0.08861	-0.07713	-0.02907
130	0.18073	-0.10674	-0.0619	-0.0316
135	0.18169	-0.12303	-0.04794	-0.0332
140	0.18558	-0.13782	-0.03538	-0.03416
145	0.1924	-0.15124	-0.02444	-0.03493
150	0.20217	-0.16309	-0.0154	-0.03601
155	0.21464	-0.17274	-0.00845	-0.0374
160	0.22804	-0.17929	-0.00293	-0.03736
165	0.23657	-0.18384	0.00215	-0.03025
170	0.23376	-0.19229	0.00506	-0.01008
175	0.23217	-0.21646	0.00317	0.00604
180	0.24038	-0.24038	0	0

Table 2. Numerical result of Mie phase function

The result phase functions for 2008 and 2010 are shown in figure 6.

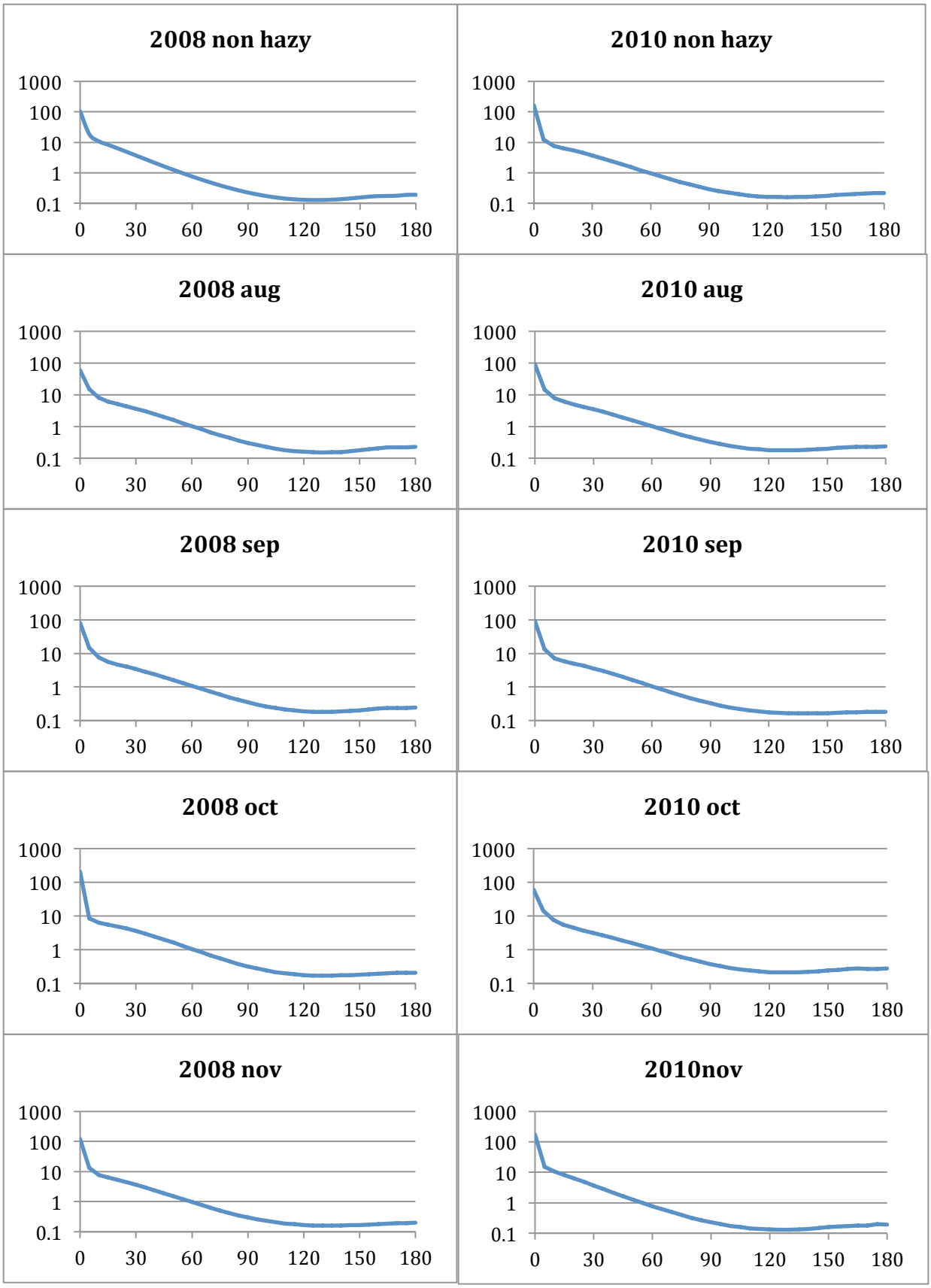

Figure 6. Mie phase functions of year 2008 and 2010

The phase function consists of two parts, forward scattering and backward scattering. The first half is from 0 to 90 degrees describe forward scattering of the atmosphere, and the other half is from 90 to 180 degrees describes backward scattering. Form the plots; it is obvious that there is no drastic change of phase function between hazy and non-hazy atmosphere. However, for months with higher small particle concentration, they show more forward scattering at very small angles (e.g. <5 degrees). This is consistent with the theory, as small particles tend to scatter light at small forward angles. The difference in backward scattering is not very obvious in these plots. This also follows the theory as haze mainly consists of small particles produced by biomass burning and hence does not affect much in the backward scattering.

The generation of Mie phase function produces not only the phase function, but also its full length Legendre expansion terms (these terms are used in the solution of the RTE). Mie scattering depends on the distribution of particle size and change in real and imaginary refractive indices. It is powerful, but also very complex. In The result for Mie scattering contains at least 400 Legendre expansion terms. Instead of writing a very complicated code and take a very long time to generate Mie phase function, there are other simpler approximation to generate similar phase functions. In this case, double Henyey-Greenstein approximation is applied to compare with Mie scattering.

3.5 Curve fitting for phase functions

In this thesis, the double Henyey-Greenstein equation is used for the approximation of phase functions. The equation takes a form of

$$P(\gamma) = f\frac{1-g_1^2}{(1+g_1^2-2g_1 cos\gamma)^{3/2}} + (1-f)\frac{1-g_2^2}{(1+g_2^2-2g_2 cos\gamma)^{3/2}} \qquad (20)$$

Curve fitting is done by MATLAB to find the fraction of forward scattering and the respective asymmetricities of forward and backward scattering. The fitting results are shown in table 3.

	2008 Nonhazy	2008 Aug	2008 Sep	2008 Oct	2008 Nov
f	0.9843	0.9876	0.9798	0.9827	0.9844
$\mathbf{g_1}$	0.7474	0.6834	0.6697	0.6847	0.6985
$\mathbf{g_2}$	-0.5425	-0.6055	-0.5158	-0.504	-0.5063
SSE	0.528	0.5371	0.7622	1.576	0.9145
R-square	0.9741	0.9679	0.9514	0.9115	0.9493
Adjusted R-square	0.9726	0.966	0.9486	0.9062	0.9464
RMSE	0.1246	0.1257	0.1497	0.2153	0.164

(a)

	2010 Nonhazy	2010 Aug	2010 Sep	2010 Oct	2010 Nov
f	0.982	0.9785	0.9901	0.9652	0.9825
$\mathbf{g_1}$	0.705	0.6843	0.6748	0.6558	0.7526
$\mathbf{g_2}$	-0.526	-0.5048	-0.5364	-0.4419	-0.5276
SSE	1.148	0.7798	0.8256	0.6272	0.8741
R-square	0.9379	0.9526	0.9522	0.9547	0.9585
Adjusted R-square	0.9342	0.9498	0.9494	0.952	0.9561
RMSE	0.1838	0.1514	0.1558	0.1358	0.1603

(b)

Table 3. Result of phase function curve fitting for (a) 2008 and (b) 2010

All the R-square results are above 0.9, showing a good approximation of the curve. Among these cases, October 2008, August 2010 and August 2008 are selected to represent the typical hazy, mixed and non-hazy conditions. These raw data are used for both Mie and double Henyey-Greenstein approximation and the phase functions generated will be compared as presented in table 4.

Weather condition	**tau**	**extinction coefficient**	**scattering coefficient**	**single scattering albedo**
non haze	0.25	0.125	0.1162505	0.930004
mix	0.50	0.250	0.22128275	0.885131
haze	0.80	0.400	0.3357204	0.839301
2008aug	0.25	0.125	0.1162505	0.930004
2010aug	0.50	0.250	0.22128275	0.885131
2008oct	0.80	0.400	0.3357204	0.839301

Table 4. Raw data for Mie and double Henyey-Greenstein phase function

4 Results and Discussions

4.1 Simulation Setting

An Atmosphere of 120km depth is set to represent the actual atmosphere, divided into 5 layers,

1. 120km: Top of the Atmosphere, Rayleigh scattering is applied
2. 10km: Rayleigh scattering
3. 2km: Mie scattering
4. 1km: Mie scattering
5. 0km: Ground level, a Lambertian reflecting surface with an albedo of 0.1.

The incoming solar flux is arbitrarily set to be $1W/m^2$ for the purpose of our simulations. The intensity distributions of solar radiation for hazy ($\sigma = 0.8$ optical depth) and non-hazy ($\sigma = 0.25\,\text{optical depth}$) atmosphere at a wavelength of 0.675 microns are simulated for both Mie and double Henyey-Greenstein phase functions at different solar angles.

In our simulation, the Mie scattering phase function involves 250 Legendre expansion terms while double Henyey-Greenstein method only uses 16 Legendre terms in the calculation. This largely reduced the length and complexity for the computation.

Below we present our simulations results for the internal radiation field as seen at ground level and computed for cases of haze and non-haze atmospheres. Special attention is give at the radiances scattered at the Almucantar plane (AP), which is the plane covering 360 degrees in the plane that is parallel to the ground and the Principal Plane (PP), which is the plane perpendicular to the ground.

4.1 Simulations of AOD at Solar Angle 30 for Clean and Hazy atmosphere.

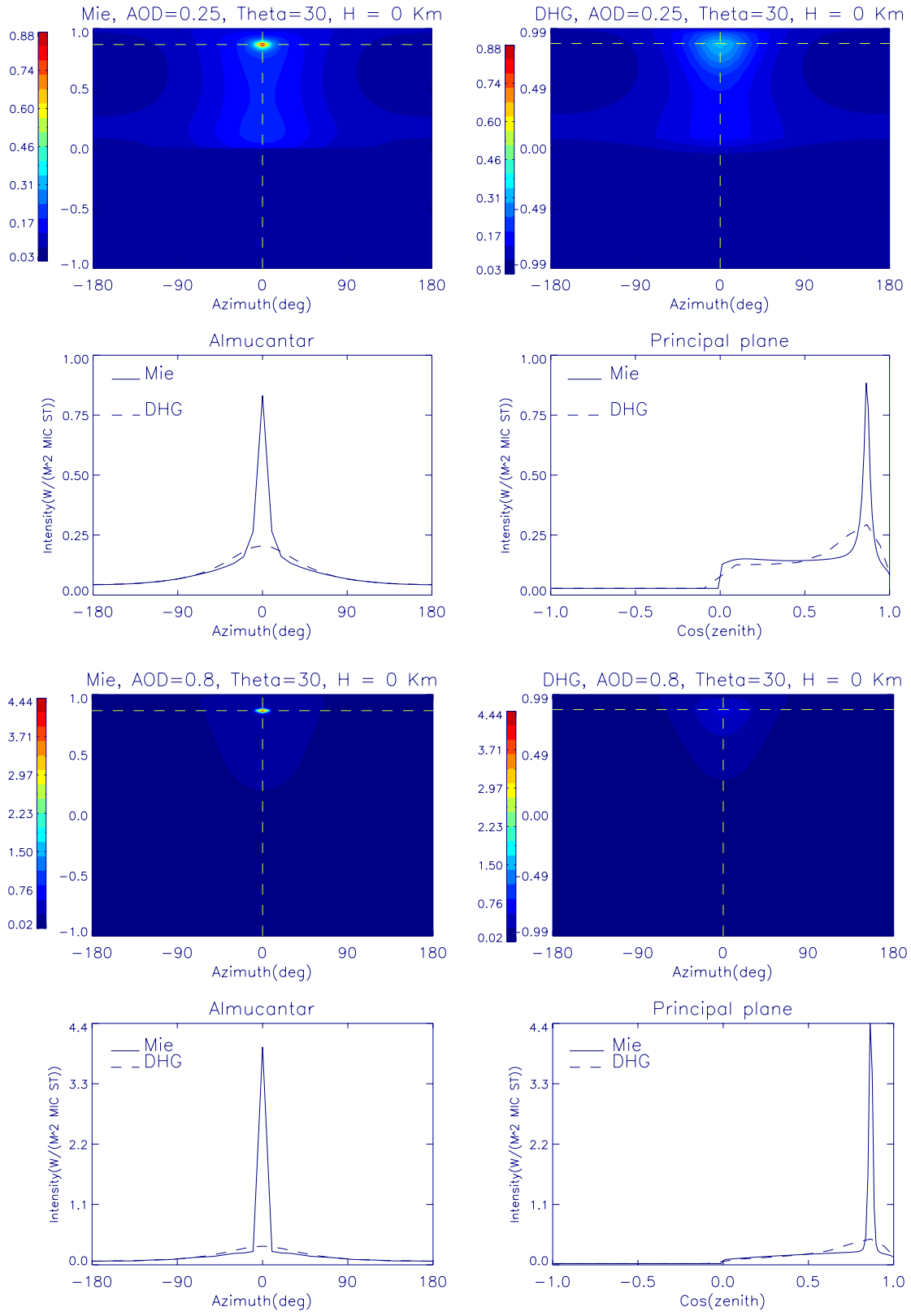

Figure 7. (a) Non-hazy atmosphere with optical depth $\sigma = 0.25$, solar angle $\theta = 30$. (b) Hazy atmosphere with optical depth $\sigma = 0.8$, solar angle $\theta = 30$.

For non-hazy atmosphere, The AP DHG graph follows the Mie scattering closely for all azimuth angles. DHG almost totally agrees with Mie for angles larger than 90 degrees but it slightly over-estimates the Mie scattering between 90 to 30 degrees. For azimuth angles between 0 to 30 degrees, the Mie scattering plot shows a very high intensity spikes at the solar aureole, which the double Henyey-Greenstein (DHG) could not reproduce. For the PP DHG plot does not fit as perfectly as the AP case. There is a slight under-estimation between 0 to 0.5 and an over-estimation above 0.5 except for the solar aureole.

For hazy atmosphere, The AP DHG plot fits even better to the Mie plot except for the spike found at solar aureole. For the PP, any under or over-estimation is not obvious Cos(zenith) from 0 to 0.5, suggesting a better fit of DHG to Mie plot. This is expected, as there is less scattering of light in hazy atmosphere and the intensities are concentrated near the solar aureole. The DHG and Mie plots agrees better near 0 zenith comparing to the non-hazy case. This may due to the reduction of the amount of solar radiation reaching the ground. When there is less solar radiation reaching the ground, the reflection of the ground is equally weak and hence there is less difference between the two plots.

It is also clear that the scattering of solar radiation is more enhanced in clean atmosphere as compared to the hazy atmosphere. For hazy atmosphere, there is a higher intensity near solar aureole but much lower intensities at large azimuth angles.

4.2 Simulations of AOD at Solar Angle 45 for Clean and Hazy atmosphere.

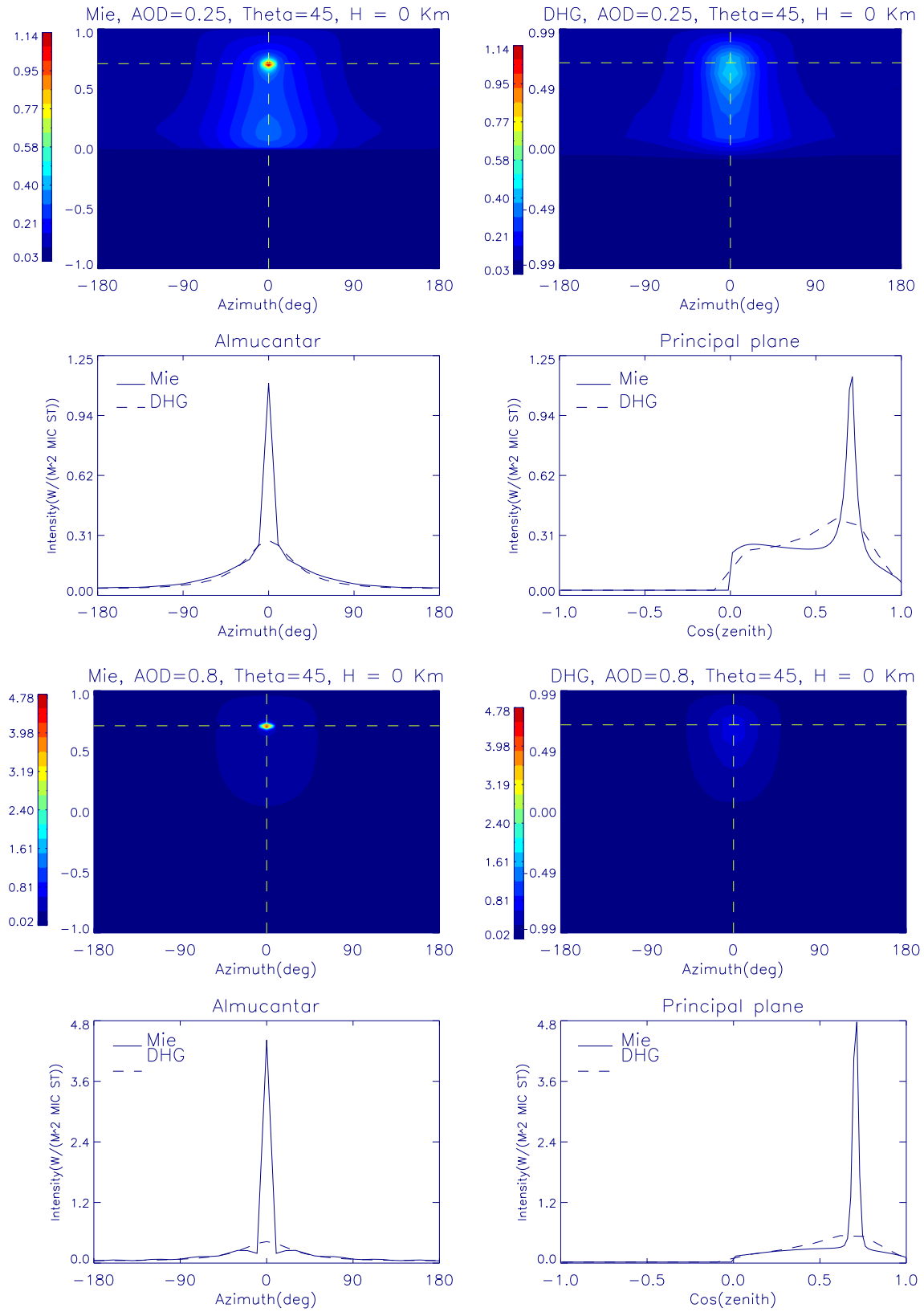

Figure 8. (a) Clean atmosphere with optical depth $\sigma = 0.25$, solar angle $\theta = 45$. (b) Hazy atmosphere with optical depth $\sigma = 0.8$, solar angle $\theta = 45$.

For clean atmosphere, The AP DHG plot follows the Mie scattering very well for most azimuth angles. For azimuth angle between 0 to 30 degrees, the Mie scattering shows a very high intensity spikes at solar aureole, which the double Henyey-Greenstein (DHG) could not reproduce (as in the previous case above) For the PP DHG case, the fit shows areas of severe under and over-estimation. There is an overestimation before Cos(zenith)=0, showing a stronger response to ground reflection than in the Mie plot case. There is a slight under-estimation between 0 to 0.3 and an over-estimation from 0.3 to 0.65 before reaching the solar aureole region. Moreover, there is an over-estimation for DHG comparing to Mie plot from Cos(zenith)~0.8 to 1. The maximum intensity peak shown in the Mie plot is not obvious in the DHG plot.

For hazy atmosphere, The AP DHG plot fits even better to the Mie plot except for the spike at solar aureole. For the PP case, the under-estimation is not obvious from 0 to 0.5, suggesting a better fit of DHG to Mie plot. This is expected, as there is less scattering of light in hazy atmosphere and the intensities are concentrated near the solar aureole. The DHG and Mie plots agrees better near 0 zenith comparing to the non-hazy case. This may due to the reduction of solar radiation reaching the ground as shown in the previous case and both the Mie and the DHG curves are more symmetrical around 0.7 in the hazy atmosphere case.

It is also clear that the solar radiation is more scattered in clean atmosphere as compared to the hazy atmosphere. For hazy atmosphere, there is a higher intensity near solar aureole but much lower intensities at large azimuth angles.

4.3 Simulations of AOD at Solar Angle 60 for Clean and Hazy atmosphere.

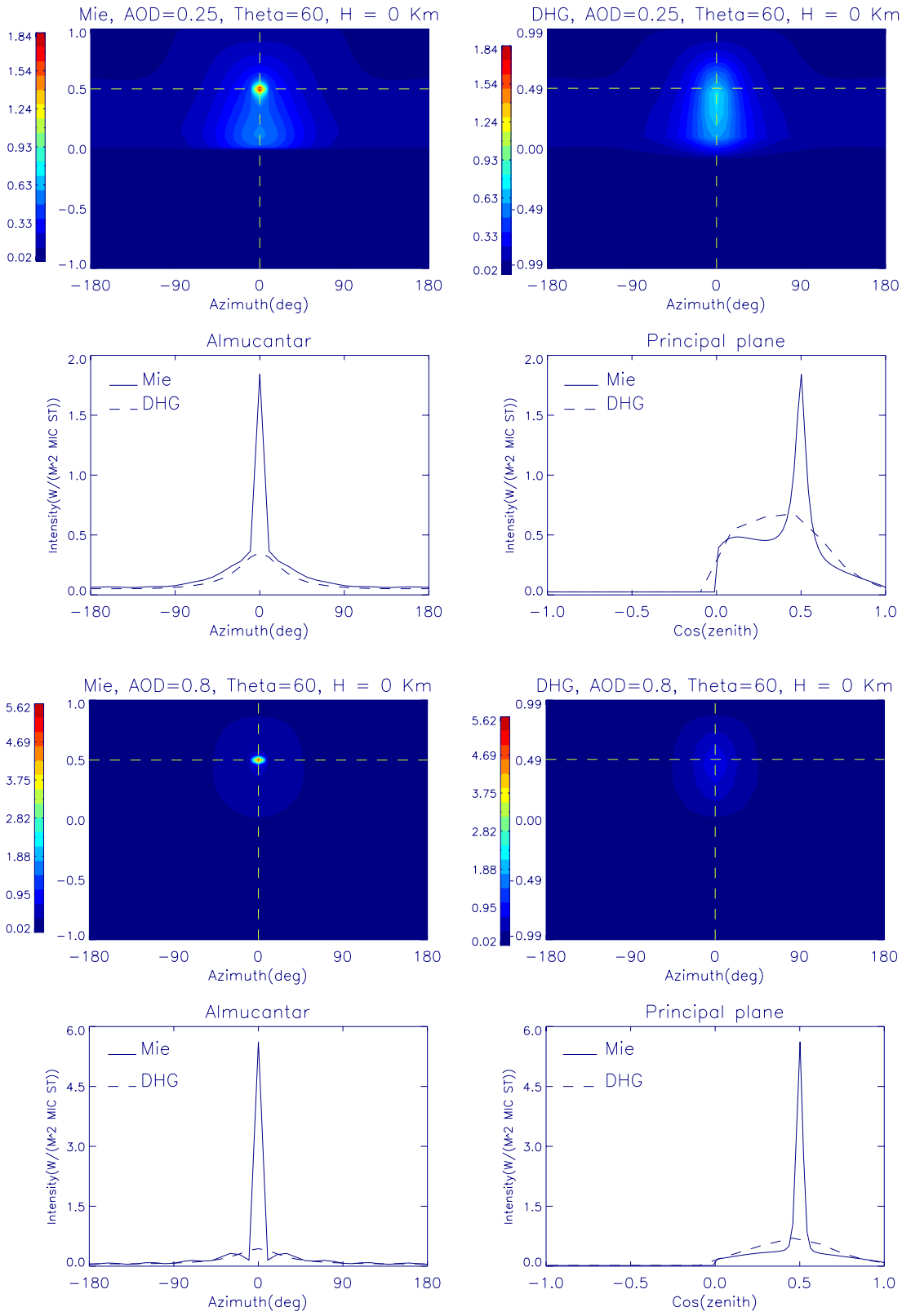

Figure 9. (a) Clean atmosphere with optical depth $\sigma = 0.25$, solar angle $\theta = 60$. (b) Hazy atmosphere with optical depth $\sigma = 0.8$, solar angle $\theta = 60$.

For non-hazy atmosphere, The AP DHG graph follows the Mie scattering very well for most azimuth angles. For azimuth angle between 0 to 30 degrees, the Mie scattering shows a very high intensity spike at solar aureole, which the double Henyey-Greenstein (DHG) could not reproduce as in the previous two cases and shows under-estimation near the solar aureole.

For the PP DHG plot does not fit as perfectly as in the AP case. There is a small over-estimation at Cos(zenith)=0, and there is almost no under-estimation from 0 to 0.5. Instead, there is an over-estimation from approximately Cos(zenith)!~0 to 0.4 before reaching the under-estimation zone near solar aureole. There is over-estimation for DHG comparing to Mie plot from Cos(zenith)~0.6 to 0.8, and a very close fit from Cos(zenith)~0.8 to 1.

For the hazy atmosphere case, The AP DHG plot fits substantially better to the Mie plot for all azimuth angles except for the spike at solar aureole. For the PP case, there is an over estimation from Cos(zenith)~0.1 to 0.4, follows by under-estimation near solar aureole, and another over-estimation from Cos(zenith)~0.6 to 0.8. Both the Mie and the DHG plot for hazy atmosphere, 60 degrees solar angle are nearly symmetrical around 0.5 due to low reflection intensity from the ground.

Overall, for the three cases shown here, the DHG does a good job representing the more complex Mie scattering term specially when looking at the Almucantar plane. Nevertheless, the goodness of fit is substantially low at the Principal plane region where areas of under- and over- estimation were observed. Moreover, the DHG fail to reproduce the distinctive forward scattering peak found at the solar aureole region. However, this is not a sever handicap as in most photometric applications, these region is avoided for all practical purposes.

5 Summary

In this thesis, 1.5 level raw data from AERONET was analyzed using Mie and radiative transfer code to generate aerosol inversions and phase functions in hazy and non-hazy atmosphere. It is noticed that in the Singapore context, the phase function does not change drastically for hazy atmosphere. However, the change in optical depth (hazy atmosphere vs. clear atmosphere) does have an impact in scattering and absorption of solar radiation as the light is more scattered in non-hazy atmosphere and is more concentrated at solar aureole for hazy-atmosphere.

The plots of double Henyey-Greenstein generally agrees with the Mie plot, expect for the spike in intensity near solar aureole. Therefore it is possible to use the DHG instead of Mie plot to reduce the computational power required to generate phase functions.

References

1. Dunbar, B. NASA – Atmospheric Aerosols: What Are They, and Why Are They So Important. 11 August 1996; Available from: http://www.nasa.gov/centers/langley/news/factsheets/Aerosols.html
2. Przyborski, P.D. Aerosols: Tiny Particles, Big Impact: Feature Articles. 11 March 2011, [last accessed on 4 April 2014] Available from: http://earthobservatory.nasa.gov/Features/Aerosols/
3. R. Balasubramanian, W.B. Qian, *Comprehensive characterization of PM2.5 aerosols in Singapore*, Journal of Geophysical Research, Vol. 108, 2003.
4. J. He, B. Zielinska and R. Balasubramanian, *Composition of semi-volatile organic compounds in the urban atmosphere of Singapore: influence of biomass burning.* Atmos. Chem. Phys., Vol. 10, p.11401-11413, 2010.
5. Computation of the Pollutant Standards Index (PSI), National Environment Agency, [last updated in March 2014]. Available from: http://www.haze.gov.sg/faq/Files/Computation%20of%20the%20Pollutant%20Standards%20Index%20(PSI).pdf
6. Craig F. Bohren and Donald R. Huffman, *Physical basis of scattering and absorption*, Absorption and Scattering of light by Small Particles, chapter1.2, p. 3-11, 1998.
7. Michael I. Mishchenko, Larry D. Travis and Andrew A. Lacis, *Scattering, Absorption, and Emission of Light by Small Particles,* Cambridge Univ. Press 2002
8. K. F. Evans and G. L. Stephens, *A new polarized atmospheric radiative transfer model*, Journal of Quantitative Spectroscopy and Radiative Transfer, Vol.46, p. 413–423, 1991.
9. Hapke B., *Theory of reflectance and emittance spectroscopy.* New York: Cambridge Univ. Press, 1993.
10. Michael I. Mishchenko, Janna M. Dlugach, Edgard G. Yanovitskij, Nadia T. Zakharova, *Bidirectional reflectance of flat, optically thick particulate layers: an efficient radiative transfer solution and applications to snow and soil surfaces.* Journal of Quantitative Spectroscopy & Radiative Transfer, Vol. 63, p.409-432, 1999.
11. Knobelspiesse, K.D., et al., *Maritime aerosol optical thickness measured by handheld sun photometers*. Remote Sensing of Environment, **93**(1-2): p.87-106, 2004.
12. Salinas, S.V., B.N. Chew, and S.C.Liew, *Retrievals of aerosol optical depth and Anstrom exponent from ground-based Sun-photometer data of Singapore*. Appl. Opt., **48**(8):p.1473-1484, 2009.
13. G. Gouesbet, T-matrix formulation and generalized Lorenz–Mie theories in spherical coordinates, Optics Communications, Vol. 283, Issue 4, p. 517-521, 2010.
14. MICHAEL I. MISHCHENKO and LARRY D. TRAVIS, *Capabilities and limitations of a current FORTRAN implementation of the T-matrix method for randomly oriented, rotationally symmetric scatterers,* Journal of Quantitative Spectroscopy and Radiative Transfer , Vol. 60, No. 3, pp. 309-324,1998.
15. R. M. Goody and Y. L Yung, *Atmospheric Radiation Theoretical Basis*, 2nd Edition (Oxford University Press, 1989)
16. Evans, K.F and Stephens, G.L, A New Radiative Transfer Model, *Journal of Quantitative*

Spectroscopy and Radiative Transfer, 1991, Volume 46,Issue 5, pp. 413 - 423
17. Dominique Toublanc, *Henyey–Greenstein and Mie phase functions in Monte Carlo radiative transfer computations.* Applied Optics, Vol. 35, Issue 18, p. 3270-3274, 1996
18. Karim Louedec and Marcel Urban, *Ramsauer approach for light scattering on nonabsorbing spherical particles and application to the Henyey–Greenstein phase function,* Applied Optics, Vol. 51, Issue 32, p. 7842-7852, 2012
19. Santo V. Salinas, Boon Ning Chew, Jukka Miettinen, et al, *Physical and optical characteristics of the October 2010 haze event over Singapore: A photometric and lidar analysis,* Atmospheric Research 122 p.555–570, 2013.
20. Santo V. Salinas, Boon N. Chew and Soo C. Liew, radiative impact of biomass burning events: The October 2010 smoke episode in South-East Asia, IGARSS 2012. p. 2536-2539